ROYAL SOCIETY
OF CHEMISTRY

Check for updates

New phases of 2D group-VA nanostructures with unusual auxetic mechanical properties induced by the regularity of the interatomic interaction force†

Hong Zheng,*[a] Zhenhan Zhao,[a] Jiasheng Chen,[a] Hanwen Qin,[a] Jun Li[a] and Xiang Zhao [iD] *[b]

Designing new auxetic materials is important for flexible electronics. The micromechanism of auxeticity in two-dimensional (2D) materials has attracted significant attention but the main factors of auxeticity are case-dependent and their connection with the geometrical/electronic features of 2D materials still requires systematic exploration. In this work, two new phases of 2D group-VA materials, namely, X10-2_2 and X12-14 (X = P, As, Sb, and Bi), were predicted. All these structures were proven to be stable from the aspects of their thermodynamic and kinetic stabilities. Investigations of their electronic properties revealed that these structures were all semiconductors with high anisotropic mobility. Mechanical analyses showed that all the X12-14 phases exhibited auxeticity, whereas the Poisson's ratios of the X10-2_2 series presented a strong dependence on the group-VA elements. The P10-2_2 structure exhibited auxeticity under both tensile and compression strain. However, As10-2_2 exhibited a peculiar half-auxeticity and Sb10-2_2 and Bi10-2_2 were non-auxetic. Evaluations of the interatomic interaction forces revealed that it is the unique folded structures and the changes of the atomic interactions that induce the different mechanical properties of the X10-2_2 structures. This work uncovers the special relationship between the auxeticity of 2D group-VA materials and the inherent natures of the group-VA elements from the viewpoint of the interatomic interaction force, which will assist future research on auxetic materials.

1. Introduction

Two-dimensional (2D) materials have attracted widespread research interest due to their excellent electronic properties and unique mechanical properties.[1] To explore more 2D materials with excellent properties, following the successful synthesis of black phosphorene (α-P),[2] the exploration of 2D phosphorous allotropes has attracted considerable interest because of the large-scale structural morphologies of phosphorous allotropes. Blue phosphorene (β-P), theoretically predicted in 2014 and experimentally synthesized by Chen and Li's group, has been revealed to feature a curved honeycomb lattice similar to silicene and found to have high carrier mobility, a suitable bandgap, and good stability.[3,4] Recently, Hittorf phosphorene (violet phosphorene) has been successfully exfoliated,[5] which is known to be more stable, less toxic, and cost-effective compared to black phosphorene. Crimson-P (violet-P_{11}), which shares a similar structure to violet phosphorene, was theoretically predicted to be stable in 2019 and successfully synthesized in 2023.[6,7] Additionally, many 2D phosphorus allotropes with various electronic properties have been proposed theoretically, including green phosphorus, γ-P, δ-P,[8] θ-P,[9] φ-P, σ-P,[10] ψ-P,[11] kagome-P,[12] O–P,[13–15] and porous phosphorus,[16] and others.[17–24] Most phosphorus monolayers exhibit a high carrier mobility and tunable bandgaps based on the number of atomic layers, making them promising candidate materials for optoelectronic devices, such as solar cells and photodetectors.[25–28] So far, the exhaustive search for 2D phosphorus allotropes has not been successful, and it remains important and valuable to continue to explore new 2D materials with novel chemical/physical properties.

Similar to phosphorous, other group-VA elements, such as arsenic, stibium, and bismuth, can also form 2D materials with similar lattice structures as phosphorenes as their sp^2 hybridization leads to analogous bonding features to phosphorous. Experimentally synthesized arsenene, antimonene, and bismuthene were reported to possess structural similarities to β-phosphorene, all exhibiting a non-planar, buckled configuration.[29–32] Concurrently, there exist many theoretically

[a]State Key Laboratory of Electrical Insulation and Power Equipment, Center of Nanomaterials for Renewable Energy, School of Electrical Engineering, Xi'an Jiaotong University, Xi'an 710049, China. E-mail: zhenghong666@xjtu.edu.cn

[b]Institute for Chemical Physics, School of Chemistry, MOE Key Laboratory for Nonequilibrium Synthesis and Modulation of Condensed Matter, Xi'an Jiaotong University, Xi'an 710049, China. E-mail: xzhao@mail.xjtu.edu.cn

stable allotropes of these two-dimensional materials that have yet to be experimentally synthesized. These unexplored allotropic forms are predicted to possess a diverse range of superior electronic and mechanical properties.[31] Despite the similar valence electronic configurations, the chemical properties of group-VA elements varies with the increasing tendencies of their atomic size and metallicity from P to Bi, which would induce different chemical and physical characteristics of 2D group-VA materials based on the same phase. Nevertheless, the influence of group-VA elements toward the electronic/mechanical properties of 2D group-VA materials has not yet been illustrated, and still requires comprehensive investigation and comparison between 2D group-VA materials based on the same conformation.

Owing to their atomic scale of thickness, the mechanical property becomes important for 2D materials and many of them have been found to exhibit auxeticity.[33] Auxeticity is reflected in the Poisson's ratio (ν), which is defined as the ratio of transverse contraction strain to longitudinal tensile strain and herein measures the fundamental mechanical response of a solid to external loads. Most materials exhibit positive Poisson's ratios, indicating that they will thin out (or thicken) laterally when subjected to longitudinal tension (or compression). By contrast, materials with negative Poisson's ratios, known as auxetic materials,[34] exhibit counterintuitive properties compared to traditional materials. Auxeticity endows nanomaterials with excellent impact resistance, superior elasticity and shear resistance, and sound/vibration absorption, leading to diverse potential applications in fields such as biomedicine, bulletproof vests, sensors, and aerospace.

Over the past decades, various negative Poisson's ratio 2D materials have been theoretically predicted, synthesized, or manufactured.[35–44] Black phosphorene is one of the most representative examples, which was predicted to possess an out-of-plane negative Poisson's ratio of -0.027.[45] Researchers attributed such an out-of-plane negative Poisson's ratio to the folded structure of black phosphorene. Subsequently, researchers have predicted multiple 2D materials with negative Poisson's ratios.[46–48] For instance, monolayer arsenene with a structure similar to black phosphorene is believed to have an out-of-plane negative Poisson's ratio of -0.09 and the magnitude becomes more negative as the number of layers increases, reaching approximately -0.12 for a four-layer arsenene.[49] δ-P was also predicted to have an in-plane negative Poisson's ratio of -0.267 due to its folded geometry.[50] Many 2D materials with geometries akin to δ-P have been suggested to possess negative Poisson's ratios, such as δ-PbO.[51] Furthermore, some 2D materials with unique auxetic properties have been proposed, such as Ag_2S with biaxial negative Poisson's ratios (in-plane and out-of-plane)[52] and PdB_4 exhibiting half-auxeticity.[53] However, to date, the number of intrinsic 2D auxetic materials remains quite limited and the search for new 2D auxetic materials remains an urgent task in modern nanodevice research. In addition, knowledge of the rules and main factors in the Poisson's ratio of auxetic materials, which strongly depend on the geometrical structures and bonding features of 2D materials, is crucial for understanding the origin of auxeticity and can only

be provided by theoretical studies. Since the phosphorus element can form various 2D materials, as mentioned above, it is possible to design auxetic 2D phosphorus materials through theoretical investigations. Moreover, other group-VA elements, such as arsenic, stibium, and bismuth, are different from phosphorus in atomic size and bonding feature, leading to possible differences in the chemical/physical properties of 2D group-VA materials, which can only be elucidated by theoretical investigations.

In this work, we first searched out a series of new phases of 2D phosphorus allotropes utilizing a structure prediction method. We then focused on two of them with unique in-plane negative Poisson's ratios and constructed analogues with other group-VA elements. The stabilities of these 2D materials were then studied from the viewpoints of cohesive energy, phonon spectrum, and *ab initio* molecular dynamics (AIMD). The electronic properties of these group-VA 2D structures were next analysed, including their band structures, partial density of states (PDOS), and carrier mobilities. For assessing their mechanical properties, the Poisson's ratios were calculated and the relationship between the Poisson's ratios and the changes among the group-VA elements was uncovered based on analyses of their geometrical structures and interatomic forces.

2. Computational methods

The search for 2D phosphorus allotropes was performed with the particle-swarm optimization (PSO) algorithm provided in the CALYPSO package.[54,55] By replacing the phosphorus atoms with arsenic, stibium, and bismuth elements, other 2D group-VA structures were constructed. In all the group-VA 2D structures, a vacuum space of 20 Å was employed to avoid interaction between the surfaces.

All the density functional theory (DFT) calculations were performed with the Vienna *Ab initio* Simulation Package (VASP).[56] In the optimizations of the 2D group-VA structures, the projector augmented wave (PAW)[57] method was used to describe the interaction between the valence electrons and core electrons. The generalized gradient approximation (GGA) with the Perdew–Burke–Ernzerhof (PBE)[58] exchange–correlation functional was used as the electronic exchange–correlation function. Convergence tests for the plane wave energy cutoff and electronic wave vector $\boldsymbol{k}$ were performed, and the appropriate wave function energy cutoff value ENCUT was set as 500 eV. The contribution of the van der Waals (vdW) interactions was considered using the DFT-D2 method developed by Grimme.[59] The Brillouin zone was sampled using mesh sizes of $5 \times 5 \times 1$ in the Γ-centered Monkhorst–Pack scheme.[60] The conjugate gradient (CG) algorithm was used to optimize the lattice structure, and convergence was reached when the Hellmann–Feynman force acting on all the unconstrained atoms was less than 0.01 eV Å^{-1} and the energy was less than 10^{-8} eV per atom. For the phonon spectrum calculations, a $3 \times 3 \times 1$ supercell was used, and the phonon spectra were obtained using the PHONOPY program.[61] In the AIMD calculations, a $3 \times 3 \times 1$ supercell was used to minimize the effect of the periodic boundary conditions. The temperature was set as room temperature (300

K) and the time step was set to 2 fs with 3000 steps, resulting in a total simulation time of 6 ps in the NVT ensemble. For the calculations of the band structures and density of states, a Gaussian broadening of 0.05 eV and the first Brillouin zone integration path were used. For orthogonal lattices, the path was $\Gamma(0.0, 0.0, 0.0) \rightarrow X(0.5, 0.0, 0.0) \rightarrow S(0.5, 0.5, 0.0) \rightarrow Y(0.0, 0.5, 0.0) \rightarrow \Gamma(0.0, 0.0, 0.0)$. Beside the PBE functional, the HSE06 hybrid functional[62] was also used for comparison in the calculations of the band structures.

The calculations of the carrier mobilities according to the deformation potential theory[63] were carried out using the following formula:[64,65]

$$\mu_{2D} = \frac{2e\hbar^3 C^{2D}}{3k_B T |m^*|^2 E_1^2} \quad (1)$$

where T is the temperature, which was set as 300 K; and m^*, C^{2D}, and k_B are the carrier's effective mass, the elastic modulus and the Boltzmann constant, respectively. The deformation potential constant E_1 for holes or electrons along a certain direction was obtained from the formula $E_1 = \Delta E/(\Delta l/l_0)$, where $\Delta l/l_0$ is the strain magnitude, and ΔE is the energy change of the valence band maximum (VBM) for holes or the conduction band minimum (CBM) for electrons. The parameter E_1 represents the shift in the band edge induced by the applied strain.

In the analyses of the mechanical properties, the Young's modulus $E(\theta)$ and Poisson's ratio $\nu(\theta)$ were calculated using the following equations:[66–69]

$$E(\theta)$$
$$= \frac{C_{11}C_{22} - C_{12}^2}{C_{11}\sin^4\theta + \left(\frac{C_{11}C_{22} - C_{12}^2}{C_{66}} - 2C_{12}\right)\sin^2\theta\cos^2\theta + C_{22}\cos^4\theta} \quad (2)$$

$$\nu(\theta) = \frac{C_{12}\sin^4\theta - \left(C_{11} + C_{22} - \frac{C_{11}C_{22} - C_{12}^2}{C_{66}}\right)\sin^2\theta\cos^2\theta + C_{12}\cos^4\theta}{C_{11}\sin^4\theta + \left(\frac{C_{11}C_{22} - C_{12}^2}{C_{66}} - 2C_{12}\right)\sin^2\theta\cos^2\theta + C_{22}\cos^4\theta} \quad (3)$$

where the C_{nn} values are the elastic constants and θ is the angle relative to the positive direction of the x-axis in plane.

3. Results and discussion

3.1. Structure and stability

By using the CALYPSO package, 15 new 2D phosphorus allotropes, which are thermodynamically and kinetically stable, were found. Details of their geometrical structures and the analyses of their stability are provided in the ESI.† In this work, two of them named P10-2_2 and P12-14 and their group-VA analogues were chosen as the study objects because of their novel mechanical properties.

In Fig. 1, the top and side views of the two phases of the group-VA monolayers together with the Wigner–Seitz cell are shown. The X10-2_2 and X12-14 phases had the space groups $P\bar{1}$ and $P2_1/c$, respectively. Herein, 10 and 12 represent the number of atoms contained in the unit cell, and 2 and 14 represent the space group serial number. The '_2' ordinal number is used to distinguish the structure of multiple identical space groups (another two phases named X10-2_1 and X10-2_3 have also been discovered). The geometrical structures of the X10-2_2 and X12-14 phases could be described as a combination of two layers of pentagonal phosphorous rings along the z axis. Specifically, in the X10-2_2 structures, each pentagonal phosphorous ring of the upper layer is connected with another neighboring ring of the lower layer by three P–P bonds, two of which form a tetragonal ring. The pentagonal phosphorous rings X12-14 structures adopt a similar layer connection through P–P bonds. For each group-VA element, the ranges of the bond length and bond angle vary little between the X10-2_2 and X12-14 phases (Table 1). As the atomic radius increases from P to Bi, the bond lengths and layer thicknesses present increasing tendencies.

To investigate the thermodynamic stability of the X10-2_2 and X12-14 structures, we first calculated their cohesive energies and compared them with other reported 2D group-VA allotropes (α and β phases), as shown in Table 2. For these 2D elemental structures, the wrinkled α phase, known as black phosphorus, was found to be the lowest-energy phase, consistent with previous studies.[70] The bulk materials of arsenene, stibnene, and bismuthene were gray arsenic, gray antimony, and β-type bismuth, respectively, corresponding to the β phase. Our calculations showed that among all the 2D group-VA structures, the E_c values of the α and β phases were rather similar ($\Delta E_c < 0.05$ eV), indicating they had similar thermodynamic stabilities.

For the X10-2_2 and X12-14 phases, their cohesive energies were higher than that of the α phase with only moderate differences (<0.15 eV). These results indicate that although both phases are metastable compared to the α and β phases, they are possible new group-VA allotropes that can exist stably. Moreover, it was revealed that the ΔE_c vales for the X10-2_2 or X12-14 phase presented a decreasing tendency going from P to Bi, suggesting the increasing tendency of their relative thermodynamic stabilities. Therefore, it is likely that the X10-2_2 and X12-14 phases could be synthesized experimentally, possibly through chemical techniques, such as epitaxial growth, colloidal suspension, or other unconventional methods.
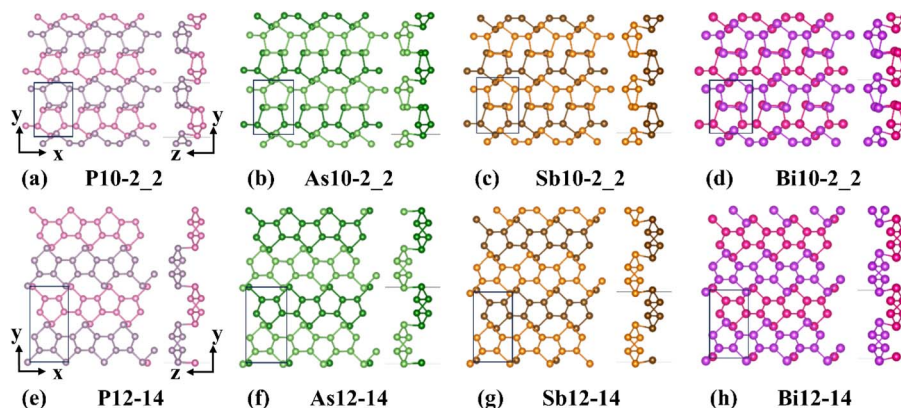
Fig. 1 (a–h) Top and side views of the X10-2_2 and X12-14 monolayers. The lower atom layers are marked with darker colors.

Table 1 Calculated values of the equilibrium lattice parameters: (a, b), thickness (h), bond lengths (d), bond angles (Y) of the X10-2_2 and X12-14 monolayers

Structure	a/Å	b/Å	γ/°	h/Å	d/Å	Y/°
P10-2_2	5.00	7.11	90	3.98	2.23–2.28	85.48–114.76
As10-2_2	5.51	7.40	90	4.51	2.49–2.52	82.62–113.92
Sb10-2_2	6.28	8.04	90	5.28	2.86–2.93	80.37–112.39
Bi10-2_2	6.61	8.16	90	5.64	3.01–3.11	79.74–111.37
P12-14	4.87	9.71	90	3.71	2.25–2.27	81.86–113.32
As12-14	5.37	10.15	90	4.18	2.49–2.52	80.00–111.73
Sb12-14	6.13	10.80	90	4.90	2.86–2.91	78.36–111.21
Bi12-14	6.47	10.98	90	4.95	3.00–3.07	77.59–108.26

Table 2 Cohesive energy (E_c)[a] and the relative cohesive energy to the α phase (ΔE_c) of the group-VA monolayers and α and β phases

Structures	E_c (eV per atom)	ΔE_c (eV per atom)
α-P	−3.608	0
β-P	−3.573	+0.035
P10-2_2	−3.482	+0.126
P12-14	−3.484	+0.124
α-As	−3.133	0
β-As	−3.128	+0.005
As10-2_2	−3.028	+0.105
As12-14	−3.039	+0.094
α-Sb	−2.879	0
β-Sb	−2.855	+0.024
Sb10-2_2	−2.799	+0.080
Sb12-14	−2.807	+0.072
α-Bi	−2.811	0
β-Bi	−2.764	+0.047
Bi10-2_2	−2.744	+0.067
Bi12-14	−2.761	+0.050

[a] $E_c = (E_{total} - n \times E_{atom})/n$, where E_{total} and E_{atom} are the total energy of the 2D group-VA allotropes and the energy of a free single atom, respectively.

To further validate the dynamical stability of these 2D structures, we calculated the phonon spectra for the X10-2_2 and X12-14 structures, as shown in Fig. S1 and S2.† All the structures exhibited no imaginary frequencies throughout the entire Brillouin zone, indicating that these structures are dynamically stable and can exist stably. The highest frequency lines and phonon band gaps of the four structures within the same phase decreased as the atomic electronegativity weakened, consistent with the trend observed in the cohesive energy changes.

Furthermore, we employed first-principles molecular dynamics (AIMD) simulations to investigate the thermal stability of these structures at room temperature. The energy variations of these structures at room temperature (300 K) are depicted in Fig. S3 and S4.† After a 6 ps simulation at room temperature, the total energies of these systems fluctuated within a very small range (<0.05 eV per atom) and they maintained their equilibrium structures almost unchanged. These results indicate that these systems can stably exist at room temperature.

3.2. Electronic structure

To investigate the electronic properties of these monolayers, the electronic band structures were determined using both the PBE and HSE06 functionals. Considering that Sb and Bi atoms are heavy atoms, the spin–orbit coupling (SOC) effect was considered. The calculated band gap values are shown in Table 3 and the band structures provided by HSE06 at ambient pressure are depicted in Fig. 2. Generally, all these structures were semiconductors and the band gaps exhibited a decreasing tendency

Table 3 Band gaps of the group-VA monolayers determined at the PBE/PBE + SOC/HSE06/HSE06 + SOC levels (eV)

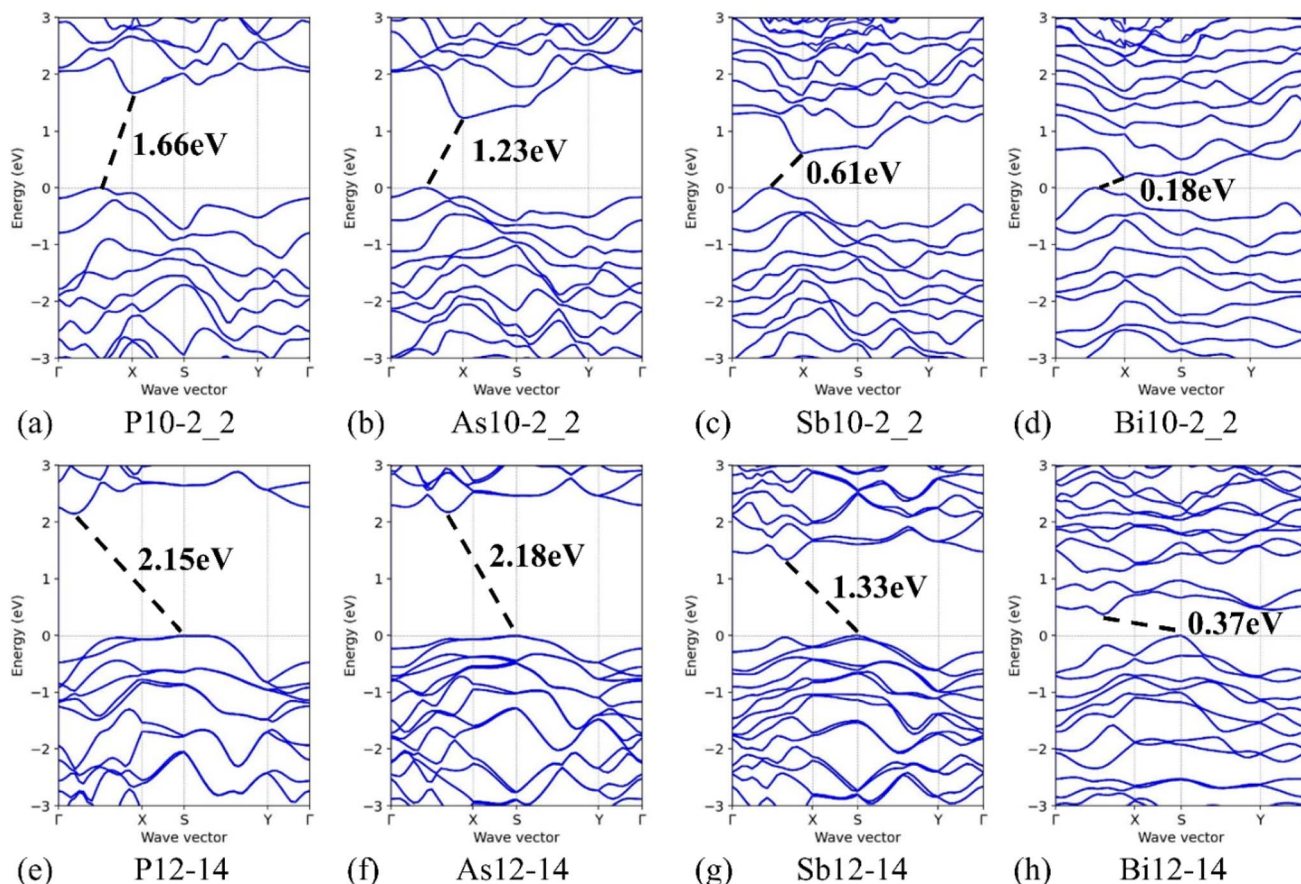| Structures	PBE (eV)	PBE + SOC (eV)	HSE06 (eV)	HSE06 + SOC (eV)
P10-2_2	0.99	0.98	1.73	1.66
As10-2_2	0.64	0.62	1.12	1.23
Sb10-2_2	0.38	0.33	0.68	0.61
Bi10-2_2	0.21	0.09	0.42	0.18
P12-14	1.40	1.39	2.14	2.15
As12-14	1.38	1.36	2.14	2.18
Sb12-14	0.95	0.90	1.38	1.33
Bi12-14	0.40	0.19	0.68	0.37

Fig. 2 Electronic band structures of the X10-2_2 phase (a–d) and the X12-14 phase (e–h).

from P to Bi in both the X10-2_2 and X12-14 phases due to their increasing metallicity. Also, the band gap values of Bi10-2_2 and Bi12-14 remarkably decreased when SOC was included, whereas SOC had little influence on the other structures. These results suggest a strong dependence of the electronic structures of the X10-2_2 and X12-14 phases on the group-VA elements. The band structures in Fig. 2 reveal that all the X10-2_2 and X12-14 phases were indirect band gap semiconductors. Fig. 2(a–d) shows that, despite the narrowed band gap from P to Bi in the X10-2_2 phase, the valence band maximum (VBM) and conduction band minimum (CBM) were located at the same k-points. Fig. 2(e–h) also shows the presence of fixed band edges in the X12-14 phase. Moreover, it could be observed that all these 2D group-VA structures had a significant number of occupied states near the Fermi level with appropriate band gaps, indicating potentially strong light absorption in the visible-light range.

In addition, the partial density of states (PDOS) was calculated for all the structures (Fig. 3), and the results were consistent with the electronic band structure results. It was revealed that the PDOS near the Fermi level for these 2D group-VA structures was mainly contributed by p orbitals due to the classic sp^3 hybridization of group-VA atoms. Specially, the VBM was mainly contributed by the p$_z$ orbital for the P and As elements, whereas it was primarily contributed by the p$_y$ orbital for the Sb and Bi elements.

3.3 Carrier mobilities

Since the X10-2_2 and X12-14 phases exhibited semiconductivity, as mentioned above, analysis of their carrier mobility, which is a significant performance index of semiconductor devices, was necessary. The carrier mobilities at $T = 300$ K were obtained and are presented in Table 4, where the superscripts/subscripts e and h represent electrons and holes, respectively. The calculated carrier mobility values indicated high anisotropy. For the X10-2_2 phase, the electron mobilities along the y direction were 15–73 times higher than those along the x direction, indicating that electrons were more likely to transmit along the y direction. Conversely, the hole mobilities were much higher along the x direction than those along the y direction. Such a change of direction preference was assigned to the deformation potential constant (E_1) term. The E_1^e value along the y direction was much smaller than that along the x direction, while the E_1^h value presented an opposite changing tendency. For the X12-14 phase, the electron mobility preferred the x direction in P12-14 and Bi12-14 but the y direction in As12-14 and Sb12-14 due to the large differences in the E_1^e values in the latter. For the hole mobilities of the X12-14 phase, all the structures preferred the x direction, which was attributed to the large elastic modulus (C^{2D}) along the x direction. Overall, due to the very small E_1^e values along the favoured direction, the electron mobility of all the X10-2_2 and X12-14 structures reaching
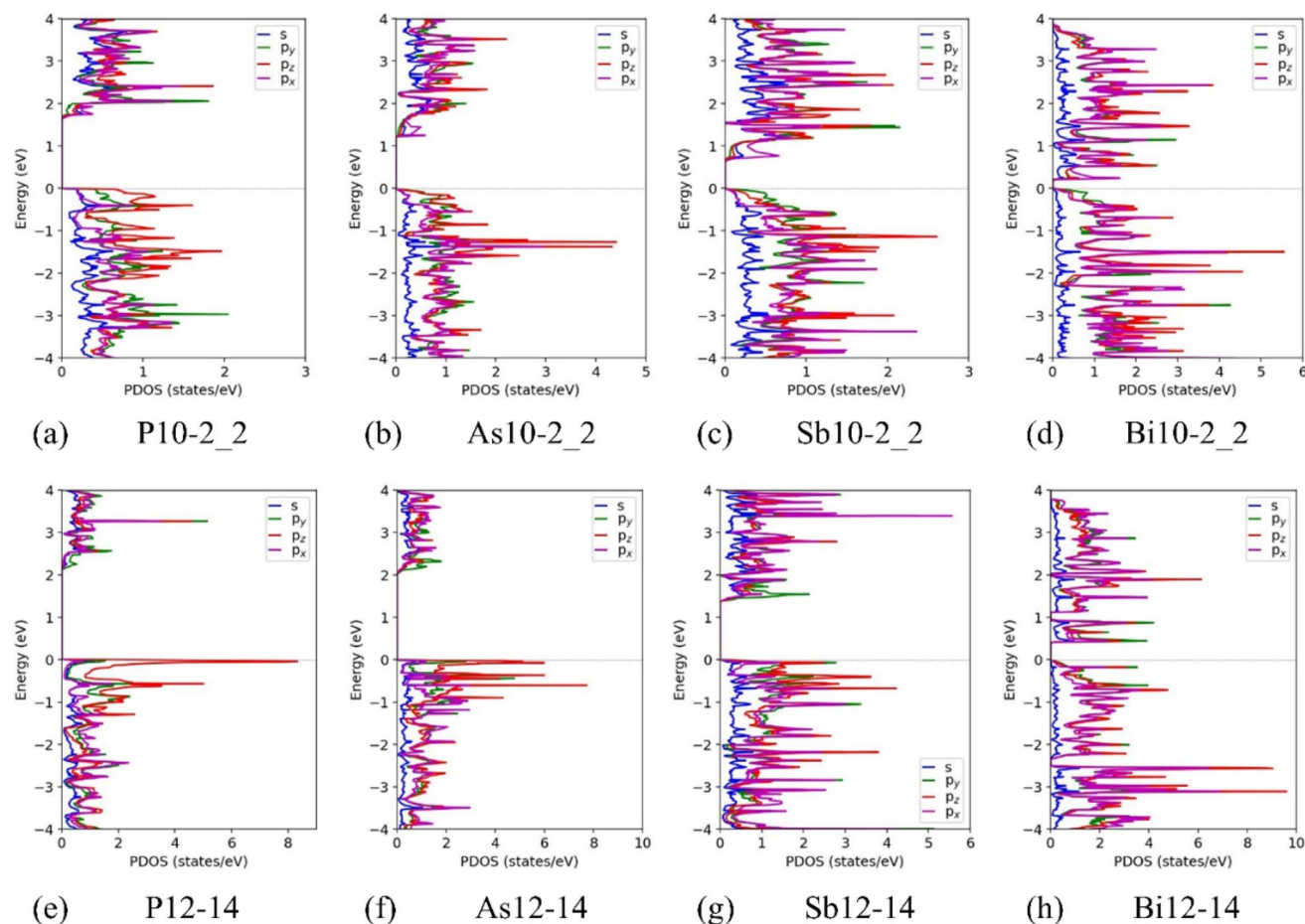
Fig. 3   PDOS of the X10-2_2 phase (a–d) and the X12-14 phase (e–h).

10^3 cm^2 V^{-1} s^{-1} was greater than the hole mobility for all the same structures. It was noteworthy that Sb10-2_2 had the highest carrier mobility of 31 493 cm^2 V^{-1} s^{-1}, even higher than the predicted carrier mobility of black phosphorus, indicating that Sb10-2_2 has potential application in nanoelectronic devices. The small E_1^e value corresponded to the localized CBM carrier density, which led to there being almost no change in the energy of these states due to the displacement of phonons.

Table 4   Elastic modulus (C^{2D}), deformation potential constant (E_1), carrier effective mass (m^*), and carrier mobility (μ) of the X10-2_2 and X12-14 phases (the superscripts/subscripts e and h represent electrons and holes, respectively)

Structure	Direc-tion	C^{2D} (J m^{-2})	E_1^e (eV)	E_1^h (eV)	$m_e^*(m_0)$	$m_h^*(m_0)$	μ_e (cm^2 V^{-1} s^{-1})	μ_h (cm^2 V^{-1} s^{-1})
P10-2_2	x	89.89	10.41	2.15	0.16	0.55	228	930
	y	14.26	0.31	3.96	0.66	0.53	9786	45
As10-2_2	x	63.75	7.50	1.59	0.13	0.45	470	2043
	y	20.92	0.51	4.46	0.57	0.34	7272	114
Sb10-2_2	x	43.65	6.25	2.13	0.13	0.31	429	1630
	y	29.07	0.28	4.26	0.60	0.23	31 493	361
Bi10-2_2	x	37.43	4.32	2.34	0.10	0.39	919	401
	y	24.47	0.53	3.04	0.93	1.00	4405	61
P12-14	x	76.64	1.31	1.17	0.26	3.45	6447	95
	y	8.37	1.40	1.22	0.57	1.70	279	19
As12-14	x	55.29	6.14	1.74	0.15	0.74	396	343
	y	7.43	0.34	1.62	0.82	1.41	3228	28
Sb12-14	x	38.25	4.84	3.55	0.12	0.20	645	357
	y	5.65	0.36	1.02	0.68	1.73	3171	76
Bi12-14	x	29.76	3.53	2.07	0.10	0.15	1894	1993
	y	6.66	1.11	0.73	0.34	0.69	1247	793

It should be noted that the deformation potential theory generally overestimates the carrier mobility because several important parameters (especially the E_1 term) are obtained by fitting and the error becomes relatively large. Also, the influence of DFT functionals toward the deformation potential constant and carrier effective mass has not been adequately analysed and discussed yet. Meanwhile, in experiments, the influence of the substrate and layer number would lead to a large deviation from an ideal 2D material. Despite all this, the absolute values of carrier mobility have poor meaning, whereas their relative values compared with those of a semiconductor material that has been proven to have high carrier conductivity (such as black phosphorus) are helpful for screening nanoelectronic devices. Therefore, in this study, we mainly compared our results with previous theoretical studies based on the same computational method.

3.4. Mechanical properties

3.4.1 Young's modulus and Poisson's ratio of X10-2_2 and X12-14. The most attractive property of X10-2_2 and X12-14 phases is their mechanical property. Here, we investigated their anisotropic mechanical performance by applying uniaxial tensile strain along the x and y directions (Fig. 1) and studied their stress–strain responses. The strain was set from +5% to +50% with an increment of 5% and the stress at each step was calculated. The stress–strain responses along the x and y directions for the two phases are shown in Fig. 4, respectively. The predicted results for the eight 2D group-VA structures showed remarkable anisotropic tensile responses with a higher tensile strength along the x direction and higher strain tolerance along the y direction. The maximum tensile strength along the x direction was larger than that along the y direction, whereas the corresponding strains of the former were much smaller than that of the latter. Specifically, the stress–strain curves of these structures along the y direction were relatively

flat, especially for Sb and Bi structures, indicating the good ductility along the y direction. Moreover, these structures could tolerate very large strains along the y direction, with As12-14 and Sb12-14 even exceeding 50%. The mechanical strength of these structures was slightly lower than that of black phosphorus (10 N m^{-1}) and comparable to that of silicon (7.2 N m^{-1}) and germanium (4.7 N m^{-1}). The elastic constants of these 2D group-VA structures are shown in Tables S1 and S2,† revealing that all eight structures satisfied the mechanical stability conditions of two-dimensional orthorhombic crystal materials: $C_{11} > 0$, $C_{11}C_{22} > C_{12}C_{12}$, $C_{66} > 0$. These results indicate the good mechanical stabilities of these structures.

Based on the numerical values of the elastic constants, the Young's modulus, Poisson's ratio, and shear modulus in all directions within the 2D plane for each structure were calculated to further elucidate the mechanical properties of these single-layer structures. The angular-dependent Young's modulus $E(\theta)$ and Poisson's ratio $\nu(\theta)$ are shown in Fig. 5 and 6. The changes in the two-dimensional polar coordinate curves indicated that the mechanical properties of all these structures were highly anisotropic. For the X10-2_2 phase, all the structures reached their maximum values in the x direction, while the maximum Young's modulus decreased in the order of P > As > Sb > Bi (Fig. 5), suggesting a weakening tendency of anisotropy. Specially, the Young's modulus of P10-2_2 reached a maximum value of 90 N m^{-1} in the x direction, comparable to the maximum Young's modulus of black phosphorus. The Young's modulus of P10-2_2 reached a minimum value of 15 N m^{-1} in the y direction, smaller than the minimum value of black phosphorus, indicating the stronger anisotropy of this structure. The X12-14 phase structures all reached their maximum values in the x direction and showed their minimum values in the y direction. Similar to X10-2_2, the four X12-14 structures also exhibited a weakening tendency of anisotropy from P to Bi.
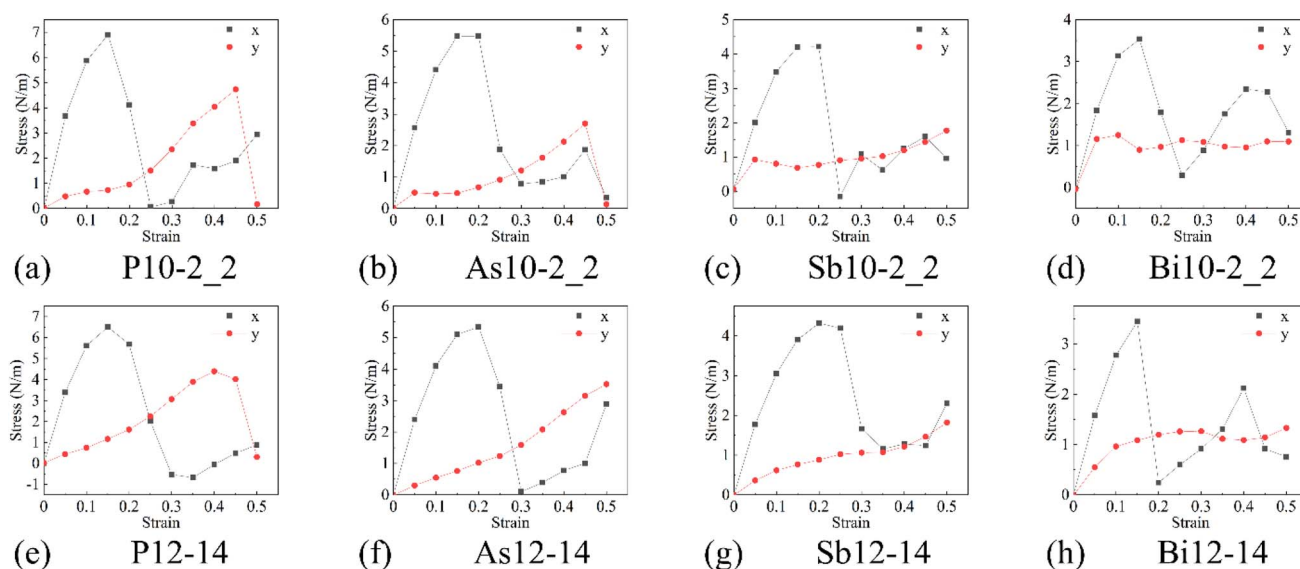

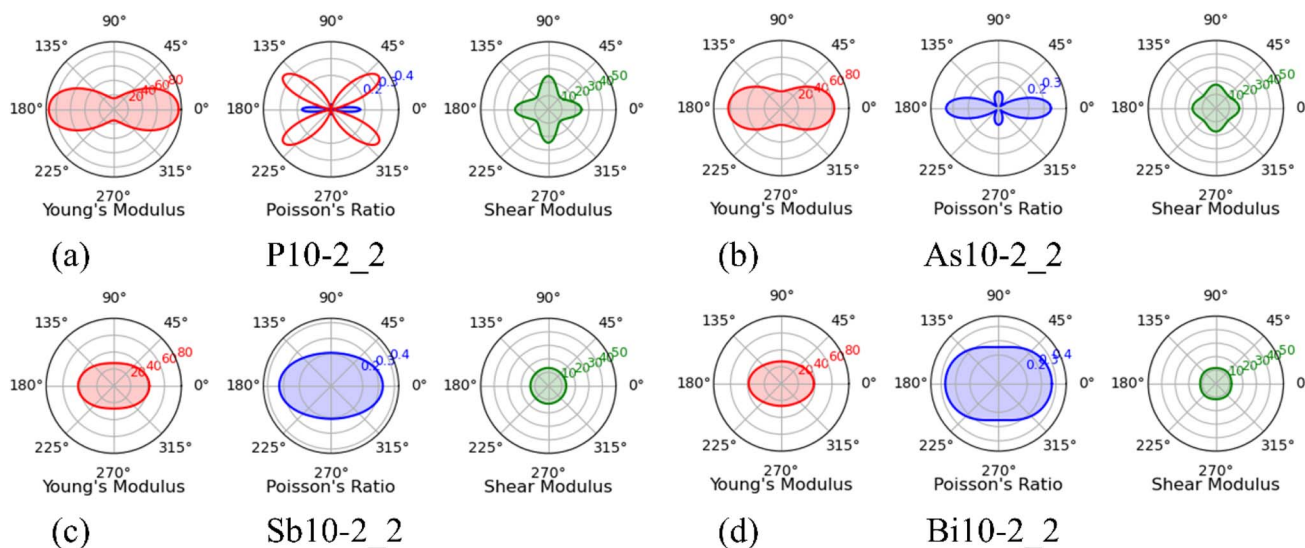Fig. 4 Stress–strain curves along the x and y directions for the X10-2_2 phase (a–d) and the X12-14 phase (e–h).

Fig. 5 Orientation dependence of the Young's modulus (in N m^{-1}), Poisson's ratio, and shear modulus (in N m^{-1}) of the X10-2_2 phase. In the pictures of the Poisson's ratio, the curves of the positive and negative Poisson's ratios are marked with blue and red colours, respectively.
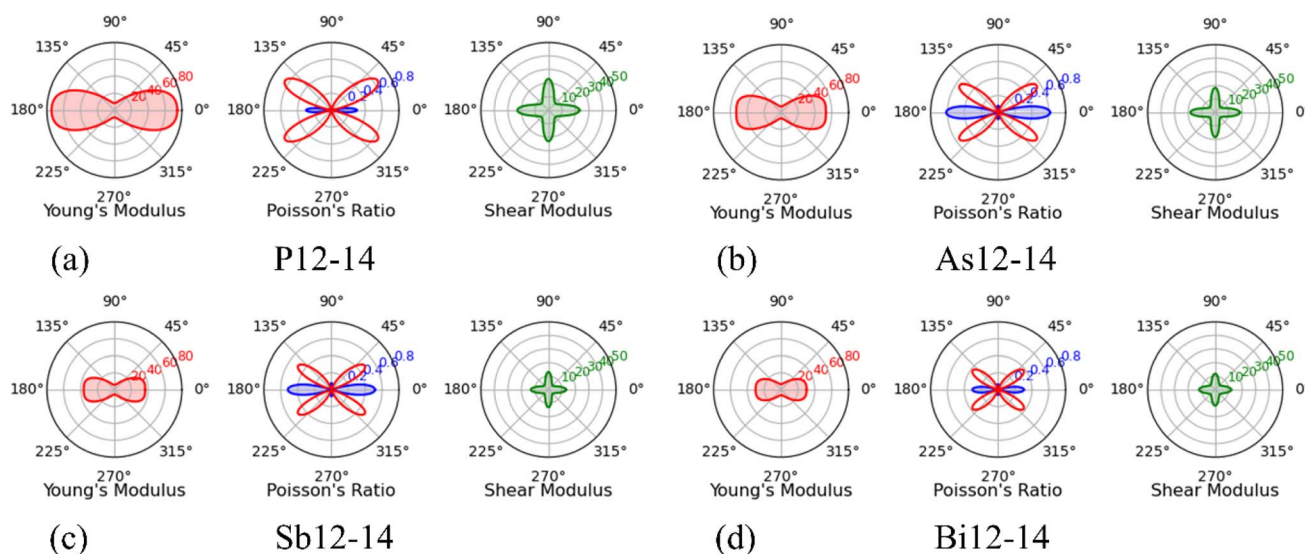

Fig. 6 Orientation dependence of the Young's modulus (in N m^{-1}), Poisson's ratio, and shear modulus (in N m^{-1}) of the X12-14 phase. In the pictures of the Poisson's ratio, the curves of the positive and negative Poisson's ratios are marked with blue and red colours, respectively.

These results also revealed that the Young's modulus values of these structures were significantly lower than those of h-BN (271 N m^{-1}) and graphene (341 N m^{-1}), and slightly lower than the maximum Young's modulus of MoS$_2$ (128 N m^{-1}), suggesting that they are relatively flexible materials. For the shear modulus, all the structures reach their minimum values at 45°, 135°, 225°, and 315° directions and maximum values in the x and y directions. Similar to the Young's modulus, the anisotropy of the shear modulus in the X10-2_2 phase weakened from P to Bi. The shear modulus values also indicated that these eight structures are relatively soft materials.

The most interesting mechanical feature of these 2D structures is their Poisson's ratio. Here, the uniaxial strains ranged

from −5% to +5%. Our calculations show that the thickness of the layer (strain along z) decreased with increasing the in-plane strain (along x and y), as shown in Fig. S5 and S6,† indicating that the out-of-plane Poisson's ratio for all the structures was positive. In the explorations of the in-plane Poisson's ratio, Fig. 5 and 6 reveal that the P10-2_2 and X12-14 structures possessed negative Poisson's ratios along the 35°, 145°, 215°, and 325° directions, ranging from −0.65 to −0.34. These NTR values are more negative than those of penta-B$_2$N$_4$ (−0.03) and α-P (−0.03). Surprisingly, the Poisson's ratio of the X10-2_2 phase exhibited a strong dependence on group-VA elements: whereby the negative Poisson's ratio disappeared in As10-2_2, Sb10-2_2, and Bi10-2_2 and the anisotropy was weakened as
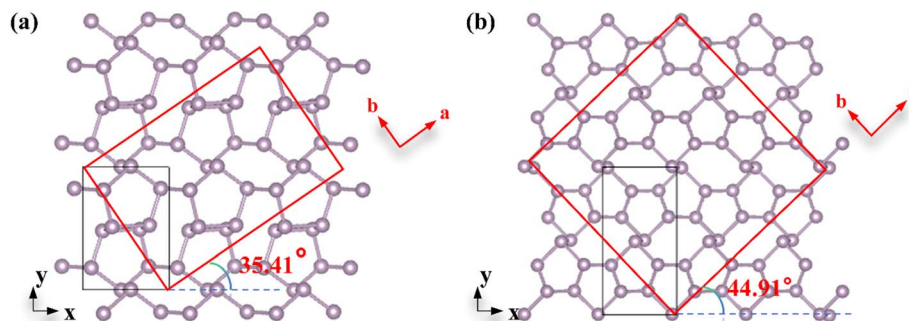
Fig. 7 Supercell (marked with red lines) used for calculating the NPR of (a) the X10-2_2 phase and (b) the X12-14 phase along the diagonal direction.

the atomic number of the group-VA element increased. All the X10-2_2 and X12-14 structures had positive Poisson's ratios along the x direction, whereas the Poisson's ratios of P10-2_2 and X12-14 along the y direction were close to 0.

Next, the uniaxial strain, defined as $\nu_{xy} = -\varepsilon_x/\varepsilon_y$, was analyzed for X10-2_2 and X12-14. Here, all the structures were deformed uniaxially along the x direction and the changes along the y direction were monitored. For the P10-2_2 and X12-14 phases, the Poisson's ratio along the y direction was slightly negative. Therefore, the expansion along the x direction resulted in no significant strain in the y direction. This is consistent with the Poisson's ratio structures obtained from the elastic constants calculations above.

3.4.2 Auxeticity along the diagonal directions. Considering the negative Poisson's ratio existing along the diagonal directions and the novel relationship between the Poisson's ratio and atomic number, we further analyzed the diagonal Poisson's ratio based on re-constructed supercells provided by matrix transformation. In the new supercells, the a direction corresponded to the array direction of the pentagonal phosphorous rings. The re-construction of the X10-2_2 phase was based on the formulae $a = 2x + y$, $b = -x + y$, while that of the X12-14 phase was based on the formulae $a = 2x + y$, $b = -2x + y$. The matrix transformations of X10-2_2 and X12-14 are shown in Fig. 7, in which the a direction of the new supercell corresponded to the 35° and 45° directions of the original X10-2_2
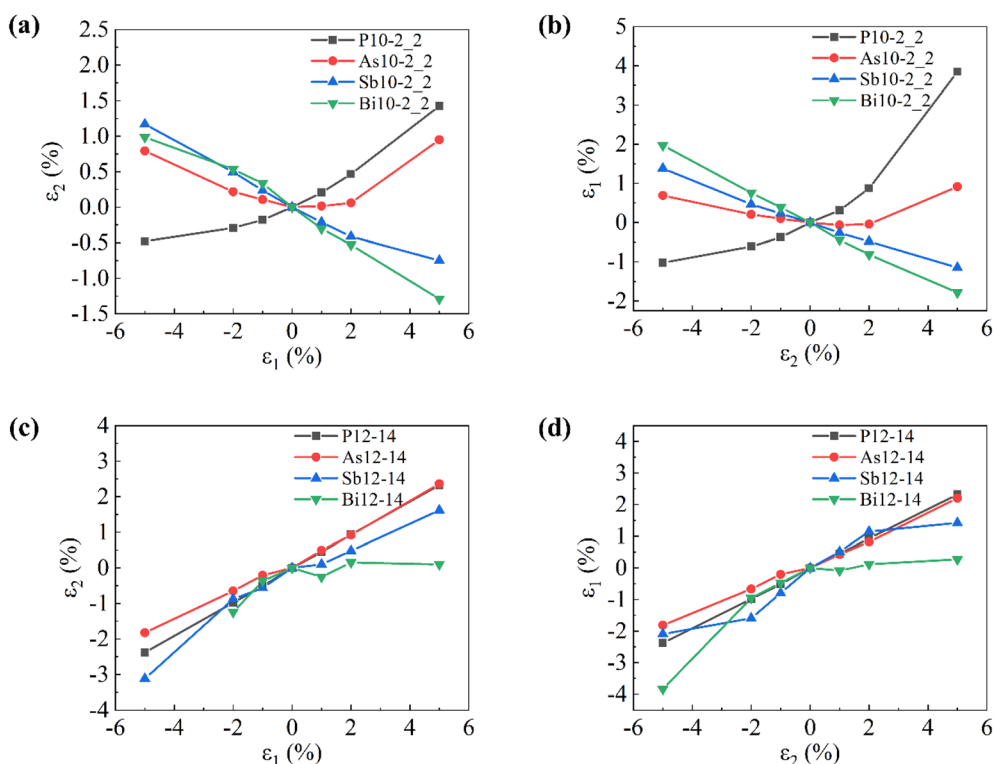

Fig. 8 Mechanical response of the X10-2_2 phase (a and b) and the X12-14 phase (c and d) under uniaxial strain along the a (ε_a) and b (ε_b) directions.

and X12-14 cells, respectively. Unlike the original cell, the newly constructed supercells were not completely orthogonal.

The corresponding strain responses along the a/b directions for the X10-2_2 and X12-14 structures are shown in Fig. 8, respectively. Due to the structural destruction in the Bi12-14 structure when applying a −5% compressive strain along the a direction, the data for this strain were omitted. The calculated strain responses were consistent with the elastic constants calculations above. All the X12-14 structures exhibited negative Poisson's ratios along both the a and b directions. The P10-2_2 structure exhibited negative Poisson's ratios along the a and b directions, while Sb10-2_2 and Bi10-2_2 exhibited positive Poisson's ratios. Specially, being similar with the case of the PdB$_4$ monolayer, the As10-2_2 structure exhibited a half-auxeticity effect; whereby it presented negative Poisson's ratios during stretching but positive Poisson's ratios during compressing. Apparently, there existed a novel relationship between the Poisson's ratio and group-VA elements in the X10-2_2 phase, which requires deeper analysis of their structures.

3.4.3 Atomic displacement directions of the X10-2_2 structures. To understand the origin of the change in Poisson's ratio in the X10-2_2 phase, the bond lengths, bond angles,

and atomic displacements of the four X10-2_2 structures under tensile and compressive strains along the a direction were analyzed. In P10-2_2, when strain was applied along the a direction, changes mainly occurred in the relative position of the upper and lower pentagon rings while the bond lengths of the P–P bond changed little (Fig. 9(a and b)). Such a geometrical change was reflected by the bond angles around the P2–P4 bond and the tetragonal ring composed of P4–P8 and P5–P9 bonds. When the strain changed from −5% to +5%, both ∠P1P2P6 and ∠P3P2P6 were enlarged by around 2°. The bond angles of the pentagon rings varied little in this process. Moreover, the angle between the P2–P4 bond and the y-axis, defined as θ, was significantly enlarged from 84.66° to 97.80° as the strain increased from −5% to +5% (Fig. 9(c–e)). Similar changes occurred in the bond angles of the tetragonal ring; whereby ∠P3P7P10 and ∠P1P8P9 were enlarged (106.78–107.31° for ∠P3P7P10 and 89.18–97.75° for ∠P1P8P9, respectively) as the strain was increased by the same extent. These geometrical changes induced oblique and nearly parallel movements in opposite directions between the two layers of pentagon rings, whose component along the b direction caused a size contraction under compressive strain and size expansion under
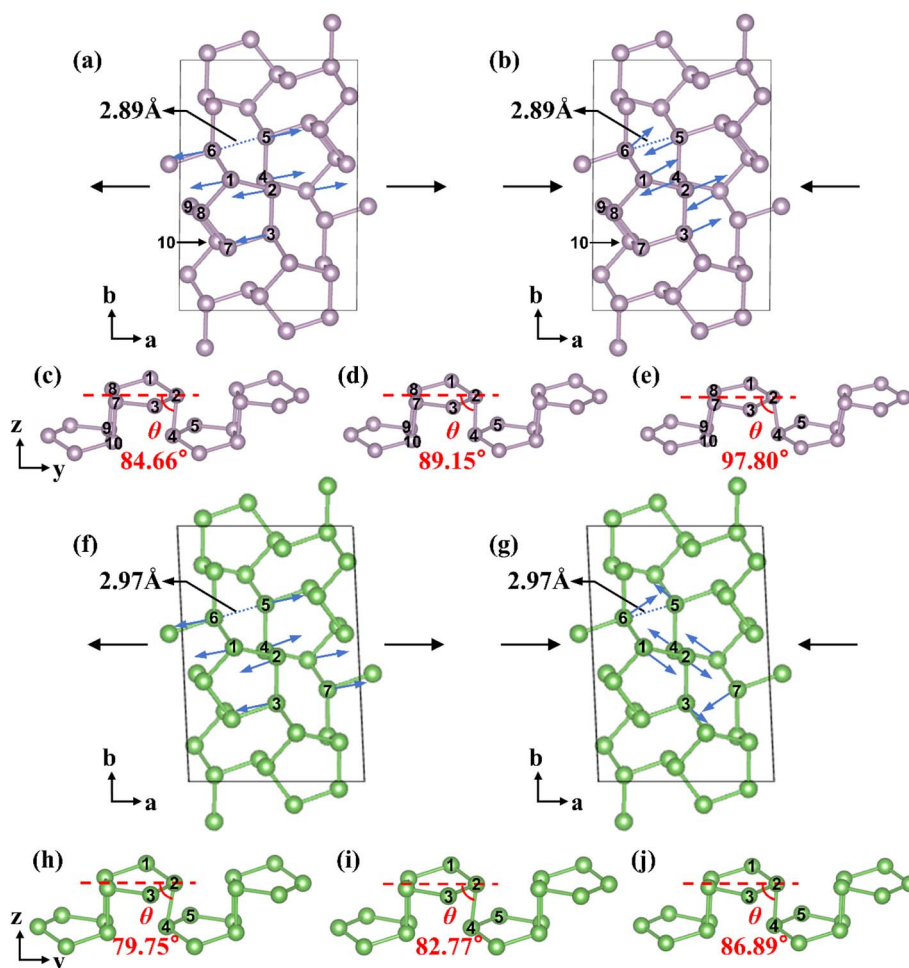

Fig. 9 Atomic displacement directions of P10-2_2 (a and b) and As10-2_2 (f and g) under tensile and compressive strain in the a direction and the side view under (c and h) −5% (d and i) 0% (e and j) +5% strain in the x direction.

expansive strain in the b direction. Generally, during stretching or compression, the P10-2_2 structure adapted to external strain mainly through changes of the bond angles rather than P–P bond lengths and herein exhibited negative Poisson's ratios.

As mentioned above, the mechanical properties of X10-2_2 (X = As, Sb, and Bi) were different from those of P10-2_2, indicating the different atomic displacements of X10-2_2 (X = As, Sb, and Bi) compared with P10-2_2. For the As10-2_2 structure, we studied its strain response and the atomic displacement changes after it experienced tensile or compressive strain along the a direction. As shown in Fig. 9(f–j), when As10-2_2 underwent tensile strain along the a direction, the atomic displacements were similar with those of P10-2_2, resulting in a negative Poisson's ratio (Fig. 9(f)). However, when As10-2_2 experienced compressive strain along the a direction, the atomic displacements became quite different from in the case of P10-2_2 (Fig. 9(g)). The b direction component in the moving directions for As1, As2, As3, and As7 were along the negative b direction, whereas those for As5, As6, and As4 were along the positive b direction. Moreover, the θ angle increased under tensile strain, similar with the case of P10-2_2, but changed little under compressive strain. The atomic displacements of Sb10-2_2 and Bi10-2_2 were different from those of P10-2_2 under both tensile and compressive strain (Fig. 10).

3.4.4 Relationship between the bonding features and mechanical properties of the X10-2_2 phase. We next wondered why the Poisson's ratio of these X10-2_2 structures exhibited a dependence on the group-VA elements. Beside the common framework in the X10-2_2 structures and the same sp^2 hybridization of the group-VA atoms, there would be certain special interior interactions in X10-2_2 (X = As, Sb, and Bi) that hinder

Fig. 10 Atomic displacement directions of Sb10-2_2 (a and b) and Bi10-2_2 (c and d) under tensile and compression strain in the a direction.

their auxeticity. We found that, in Sb10-2_2 and Bi10-2_2, the X5–X6 distances were quite close to the formal X–X bonds (Fig. 10). The Sb5–Sb6 and Bi5–Bi6 distances were 0.2–0.4 Å larger than the Sb–Sb and Bi–Bi bonds (Table 1) under strain ranging from −5% to +5%. In As10-2_2, the As5–As6 distance was ∼0.4 Å larger than the As–As bond length under a strain of −5%. This difference was increased to ∼0.5 Å and ∼0.7 Å under the cases of no strain and a strain of +5%, respectively. In P10-2_2, the P5–P6 distance was 0.5–0.9 Å larger than the P–P bonds under strain ranging from −5% to +5%. Therefore, we deduced that, in Sb10-2_2 and Bi10-2_2 and compressed As10-2_2, the atomic interactions between the X5 and X6 atoms change the atomic displacements and induce positive Poisson's ratios. To verify this hypothesis, we calculated the negative integrated crystal orbital Hamilton population (−ICOHP) between the X5 and X6 atoms under strain for the four X10-2_2 structures. The larger the −ICOHP value between the two atoms, the stronger the interatomic interaction force. The −ICOHP values between the X5 and X6 atoms under strain along the a direction, as well as the strain responses, are shown in Fig. 11.

It was revealed that the −ICOHP value between the X5 and X6 atoms increased in the order of P < As < Sb < Bi under the case of no strain, suggesting an increasing tendency of bonding features between X5 and X6. When strain was applied, this −ICOHP value showed a decreasing tendency from the −ICOHP value between P5 and P6 from a compressive strain of −5% to a tensile strain of +5%. In P10-2_2, the −ICOHP between the P5 and P6 atoms showed a decreasing range from 1.0 eV under a strain of −5% to 0.8 eV when the strain was increased to −2%. In As10-2_2, the −ICOHP value between the As5 and As6 atoms was above 0.9 eV under compressive strain, and correspondingly, was below 0.9 eV under tensile strain, the former corresponded to negative correlations between ε_a and ε_b (positive Poisson's ratio) while the latter corresponded to positive correlations between ε_a and ε_b (negative Poisson's ratio). As for Sb10-2_2 and Bi10-2_2, the −ICOHP value stayed above 0.9 eV over the whole changing process of strain, corresponding to negative correlations between ε_a and ε_b. The −ICOHP values and the strain responses along the b direction are shown in Fig. S7,† which exhibited quite similar results to those in Fig. 11. Therefore, it could be concluded that an −ICOHP value of ∼0.9 eV is a critical point determining the auxeticity of X10-2_2. Of course this −ICOHP value is just a reference but it shows the dependence of auxeticity on the bonding between the X5 and X6 atoms. The weak bonding between X5 and X6 (such as in P10-2_2 and stretched As10-2_2) had little influence on the movement of the upper and lower pentagon rings mentioned above, resulting in negative Poisson's ratios. Nevertheless, if this interatomic interaction becomes strong, compression and stretching of the X5-X6 bond are difficult and the atomic displacements of the upper and lower pentagon rings become less flexible. Consequently, other atoms have to adjust their moving directions and the movements with opposite directions between the upper and lower pentagon rings are destroyed.

In short, the weak interatomic interaction between the X5 and X6 atoms in P10-2_2 and stretched As10-2_2 induced negative Poisson's ratios, whereas the strong interatomic
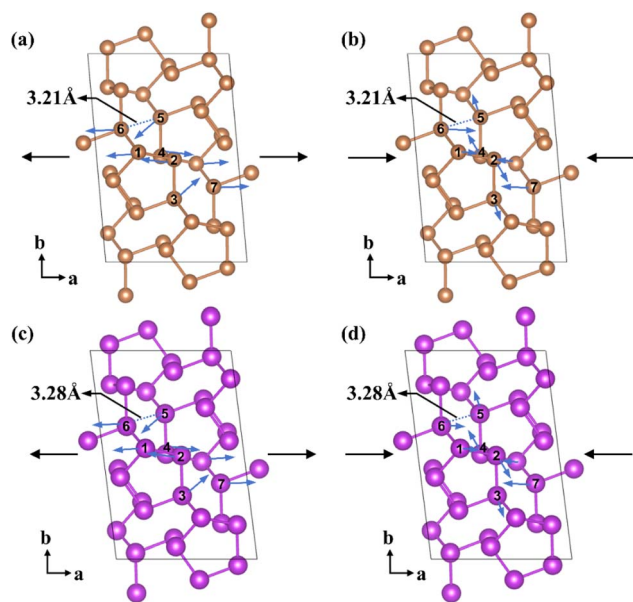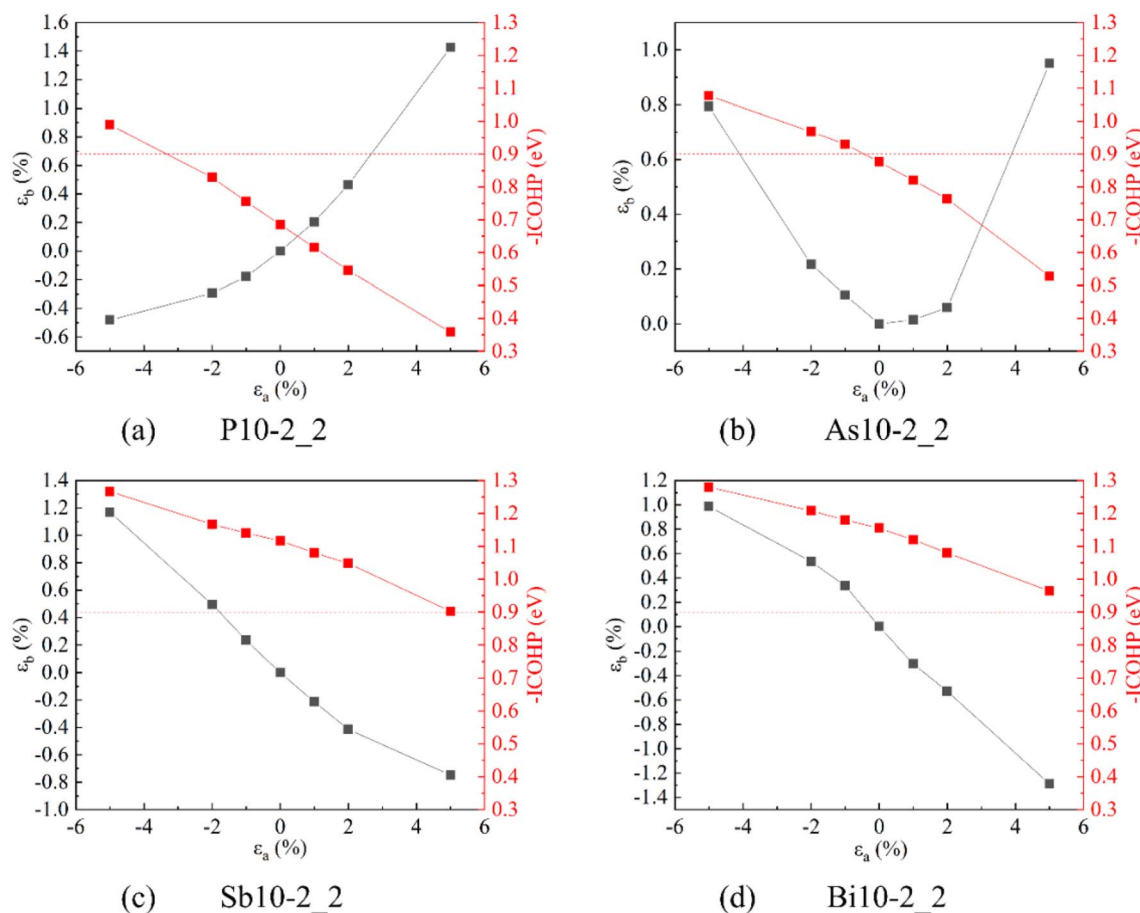
Fig. 11 Mechanical responses of the X10-2_2 phase under strain along the *a* direction (black lines) and the −ICOHP between X5 and X6 (red lines).

interaction between them in Sb10-2_2, Bi10-2_2, and compressed As10-2_2 induced positive Poisson's ratios. The increasing tendency of this interatomic interaction from P to Bi is connected with the large extension of the valence orbitals of heavy atoms, which increases the orbital overlap between the X5 and X6 atoms. Such interatomic interaction regularly increasing from non-bonding to partial bonding along with the change of group-VA elements was not found in the X12-14 phase and herein all the four X12-14 structures had negative Poisson's ratios.

4. Conclusions

In this work, two new phases of 2D group-VA materials, namely X10-2_2 and X12-14 (X = P, As, Sb, and Bi), were predicted and systematically studied. Based on calculations of the cohesive energies, phonon spectra, molecular dynamics simulations, and elastic constant, these eight structures were found to be stable from the viewpoint of both thermodynamic and kinetic stability, suggesting the good possibilities of their existence.

Analyses of the electronic structures of the X10-2_2 and X12-14 structures revealed that they are all indirect bandgap semiconductors. The structures with the same phase had similar band structures but the bandgaps decreased in the order of P >

As > Sb > Bi. All these structures had high electron mobility, especially the Sb10-2_2 structure with an electron mobility of 31 493 cm^2 V^{-1} s^{-1} along the *y* direction, making them suitable for nanoelectronic devices.

In addition, analyses of the uniaxial tensile strain, Young's modulus, and Poisson's ratio disclosed that these materials possessed unique mechanical properties. Both X10-2_2 and X12-14 phases were stable, soft, and anisotropic materials. Analysis of the diagonal Poisson's ratio suggested that the four X12-14 structures exhibited in-plane negative Poisson's ratios. For the X10-2_2 phase, the P10-2_2 structure exhibited in-plane negative Poisson's ratios in the 35° and 145° directions, while the As10-2_2 structure exhibited half-auxeticity. The Sb10-2_2 and Bi10-2_2 structures exhibited positive Poisson's ratios. It was found that the strengthened atomic interactions between the atoms of the upper and lower pentagon rings led to positive Poisson's ratio in Sb10-2_2, Bi10-2_2, and compressed As10-2_2. Such atomic interactions for As, Sb, and Bi elements were assigned to their large extension of valence orbitals, which increases atomic orbital overlap. These results are valuable for the designation of auxetic nanomaterials and for expanding their potential applications in the fields of flexible electronics, biomedicine, protection devices, aerospace, nanosensors, *et al.*

Data availability

The data supporting the findings of this article are included in the ESI.†

Conflicts of interest

The authors declare no competing financial or non-financial interests.

Acknowledgements

References

1 H. Zhang, *ACS Nano*, 2015, **9**, 9451–9469.

2 L. K. Li, Y. J. Yu, G. J. Ye, Q. Q. Ge, X. D. Ou, H. Wu, D. L. Feng, X. H. Chen and Y. B. Zhang, *Nat. Nanotechnol.*, 2014, **9**, 372–377.

3 Z. Zhu and D. Tomanek, *Phys. Rev. Lett.*, 2014, **112**, 176802.

4 J. L. Zhang, S. Zhao, S. Sun, H. Ding, J. Hu, Y. Li, Q. Xu, X. Yu, M. Telychko, J. Su, C. Gu, Y. Zheng, X. Lian, Z. Ma, R. Guo, J. Lu, Z. Sun, J. Zhu, Z. Li and W. Chen, *ACS Nano*, 2020, **14**, 3687–3695.

5 L. Zhang, H. Huang, B. Zhang, M. Gu, D. Zhao, X. Zhao, L. Li, J. Zhou, K. Wu, Y. Cheng and J. Zhang, *Angew. Chem.*, 2020, **59**, 1074–1080.

6 H. Huang, L. Zhang, B. Xiao, Y. Cheng and J. Zhang, *Appl. Phys. Lett.*, 2019, **115**, 163101.

7 G. Cicirello, M. Wang, Q. P. Sam, J. L. Hart, N. L. Williams, H. Yin, J. J. Cha and J. Wang, *J. Am. Chem. Soc.*, 2023, **145**, 8218–8230.

8 J. Guan, Z. Zhu and D. Tomanek, *Phys. Rev. Lett.*, 2014, **113**, 046804.

9 M. Wu, H. Fu, L. Zhou, K. Yao and X. C. Zeng, *Nano Lett.*, 2015, **15**, 3557–3562.

10 P. G. Demingos and A. R. Muniz, *J. Phys. Chem. C*, 2020, **124**, 21207–21214.

11 H. Wang, X. Li, Z. Liu and J. Yang, *Phys. Chem. Chem. Phys.*, 2017, **19**, 2402–2408.

12 G. Yu, L. Jiang and Y. Zheng, *J. Phys.: Condens. Matter*, 2015, **27**, 255006.

13 P. Li and W. Luo, *Sci. Rep.*, 2016, **6**, 25423.

14 F. Ersan, E. Aktürk and S. Ciraci, *Phys. Rev. B:Condens. Matter Mater. Phys.*, 2016, **94**, 245417.

15 G. Barik and S. Pal, *Phys. Chem. Chem. Phys.*, 2021, **23**, 26547–26560.

16 Z. Zhuo, X. Wu and J. Yang, *J. Am. Chem. Soc.*, 2016, **138**, 7091–7098.

17 T. Zhao, C. Y. He, S. Y. Ma, K. W. Zhang, X. Y. Peng, G. F. Xie and J. X. Zhong, *J. Phys.: Condens. Matter*, 2015, **27**, 265301.

18 M. Xu, C. He, C. Zhang, C. Tang and J. Zhong, *Phys. Status Solidi RRL*, 2016, **10**, 563–565.

19 M. Maatallah and A. Jarid, *Chem. Phys.*, 2019, **516**, 103–107.

20 J. Liu, Y. Guo, S. Zhang, Q. Wang, Y. Kawazoe and P. Jena, *J. Phys. Chem. C*, 2015, **119**, 24674–24680.

21 S. Kaur, A. Kumar, S. Srivastava, K. Tankeshwar and R. Pandey, *Nanotechnology*, 2020, **31**, 325702.

22 W. H. Han, S. Kim, I. H. Lee and K. J. Chang, *J. Phys. Chem. Lett.*, 2017, **8**, 4627–4632.

23 W. Geng, J. Xiao, J. J. Brown, A. J. Page and Z. Ke, *J. Phys. Chem. C*, 2019, **123**, 10788–10794.

24 C. Dai, X. Cai, Y. Ni, Y. Chen and H. Wang, *Phys. Chem. Chem. Phys.*, 2022, **24**, 22572–22579.

25 S. Kaur, A. Kumar, S. Srivastava, R. Pandey and K. Tankeshwar, *Nanotechnology*, 2018, **29**, 155701.

26 Y. Wang, S. Sun, J. Zhang, Y. L. Huang and W. Chen, *SmartMat*, 2021, **2**, 286–298.

27 X. Han, J. Han, C. Liu and J. Sun, *Adv. Funct. Mater.*, 2018, **28**, 1803471.

28 C. Li, L. He, X. Li, J. Luo, X. Zhu, Z. Chen and M. Xu, *J. Mater. Chem. C*, 2021, **9**, 6802–6814.

29 S. L. Zhang, Z. Yan, Y. F. Li, Z. F. Chen and H. B. Zeng, *Angew. Chem., Int. Ed.*, 2015, **54**, 3112–3115.

30 J. P. Ji, X. F. Song, J. Z. Liu, Z. Yan, C. X. Huo, S. L. Zhang, M. Su, L. Liao, W. H. Wang, Z. H. Ni, Y. F. Hao and H. B. Zeng, *Nat. Commun.*, 2016, **7**, 13352.

31 M. Pumera and Z. Sofer, *Adv. Mater.*, 2017, **29**, 1605299.

32 F. Reis, G. Li, L. Dudy, M. Bauernfeind, S. Glass, W. Hanke, R. Thomale, J. Schafer and R. Claessen, *Science*, 2017, **357**, 287–290.

33 R. Peng, Y. D. Ma, Q. Wu, B. B. Huang and Y. Dai, *Nanoscale*, 2019, **11**, 11413–11428.

34 K. E. Evans, *Endeavour*, 1991, **15**, 170–174.

35 L. Yu, Y. Wang, X. Zheng, H. Wang, Z. Qin and G. Qin, *Appl. Surf. Sci.*, 2023, **610**, 155478.

36 G. Qin and Z. Qin, *npj Comput. Mater.*, 2020, **6**, 51.

37 K. W. Wojciechowski, *Mol. Phys.*, 1987, **61**, 1247–1258.

38 K. W. Wojciechowski, *Phys. Lett. A*, 1989, **137**, 60–64.

39 K. E. Evans and M. A. Nkansah, *Nature*, 1991, **353**, 124.

40 J. N. Grima and K. E. Evans, *J. Mater. Sci. Lett.*, 2000, **19**, 1563–1565.

41 K. W. Wojciechowski, *J. Phys. A: Math. Gen.*, 2003, **36**, 11765.

42 J. N. Grima, S. Winczewski, L. Mizzi, M. C. Grech, R. Cauchi, R. Gatt, D. Attard, K. W. Wojciechowski and J. Rybicki, *Adv. Mater.*, 2015, **27**, 1455–1459.

43 W. Gong and Q. Yan, *Comput. Mater. Sci.*, 2021, **195**, 110332.

44 T.-C. Lim, *Int. J. Solids Struct.*, 2024, **305**, 113095.

45 J.-W. Jiang and H. S. Park, *Nat. Commun.*, 2014, **5**, 4727.

46 L. Yu, Q. Yan and A. Ruzsinszky, *Nat. Commun.*, 2017, **8**, 15224.

47 J. Pan, Y.-F. Zhang, J. Zhang, H. Banjade, J. Yu, L. Yu, S. Du, A. Ruzsinszky, Z. Hu and Q. Yan, *npj Comput. Mater.*, 2020, **6**, 154.

48 T. Jing, D. Liang, M. Deng and S. Cai, *J. Mater. Chem. C*, 2020, **8**, 10382–10389.

49 J. W. Han, J. F. Xie, Z. Y. Zhang, D. Z. Yang, M. S. Si and D. S. Xue, *Appl. Phys. Express*, 2015, **8**, 041801.

50 H. D. Wang, X. X. Li, P. Li and J. L. Yang, *Nanoscale*, 2017, **9**, 850–855.

51 S. Xu, X. Ma, Y. Li, Y. Qu and M. Zhao, *ACS Appl. Electron. Mater.*, 2022, **4**, 2264–2271.

52 R. Peng, Y. Ma, Z. He, B. Huang, L. Kou and Y. Dai, *Nano Lett.*, 2019, **19**, 1227–1233.

53 F. Ma, Y. Jiao, W. Wu, Y. Liu, S. A. Yang and T. Heine, *Nano Lett.*, 2021, **21**, 2356–2362.

54 Y. C. Wang, J. Lv, L. Zhu and Y. M. Ma, *Comput. Phys. Commun.*, 2012, **183**, 2063–2070.

55 Y. Wang, M. Miao, J. Lv, L. Zhu, K. Yin, H. Liu and Y. Ma, *J. Chem. Phys.*, 2012, **137**, 224108.

56 G. Kresse and J. Furthmuller, *Phys. Rev. B:Condens. Matter Mater. Phys.*, 1996, **54**, 11169–11186.

57 P. E. Blochl, *Phys. Rev. B:Condens. Matter Mater. Phys.*, 1994, **50**, 17953–17979.

58 J. P. Perdew, K. Burke and M. Ernzerhof, *Phys. Rev. Lett.*, 1996, **77**, 3865–3868.

59 S. Grimme, *J. Comput. Chem.*, 2006, **27**, 1787–1799.

60 H. J. Monkhorst and J. D. Pack, *Phys. Rev. B*, 1976, **13**, 5188–5192.

61 A. Togo, *J. Phys. Soc. Jpn.*, 2023, **92**, 012001.

62 J. Heyd, G. E. Scuseria and M. Ernzerhof, *J. Chem. Phys.*, 2003, **118**, 8207–8215.

63 J. Bardeen and W. Shockley, *Phys. Rev.*, 1950, **80**, 72–80.

64 J. Qiao, X. Kong, Z.-X. Hu, F. Yang and W. Ji, *Nat. Commun.*, 2014, **5**, 4475–4481.

65 H. Lang, S. Zhang and Z. Liu, *Phys. Rev. B:Condens. Matter Mater. Phys.*, 2016, **94**, 235306.

66 C. Jasiukiewicz, T. Paszkiewicz and S. Wolski, *Phys. Status Solidi B*, 2008, **245**, 557–561.

67 V. Wang, N. Xu, J.-C. Liu, G. Tang and W.-T. Geng, *Comput. Phys. Commun.*, 2021, **267**, 108033.

68 K. W. Wojciechowski, *Comput. Methods Sci. Technol.*, 2005, **11**, 73–79.

69 M. Bilski, P. M. Pigłowski and K. W. Wojciechowski, *Symmetry*, 2021, **13**, 1127.

70 S. Zhang, M. Xie, F. Li, Z. Yan, Y. Li, E. Kan, W. Liu, Z. Chen and H. Zeng, *Angew. Chem.*, 2015, **128**, 1698–1701.